RESEARCH ARTICLE

Voxel level quantification of [11C]CURB, a radioligand for Fatty Acid Amide Hydrolase, using high resolution positron emission tomography

Pablo M. Rusjan[1,2]*, Dunja Knezevic[1], Isabelle Boileau[1,2], Junchao Tong[1,2], Romina Mizrahi[1,2], Alan A. Wilson[1,2], Sylvain Houle[1,2]

1 Research Imaging Centre, CAMH Campbell Family Mental Health Research Institute, Toronto, Ontario, Canada, 2 Department of Psychiatry, University of Toronto, Toronto, Ontario, Canada

* pablo.rusjan@camhpet.ca

Abstract

[11C]CURB is a novel irreversible radioligand for imaging fatty acid amide hydrolase in the human brain. In the present work, we validate an algorithm for generating parametric map images of [11C]CURB acquired with a high resolution research tomograph (HRRT) scanner. This algorithm applies the basis function method on an irreversible two-tissue compartment model ($k_4 = 0$) with arterial input function, i.e., BAFPIC. Monte Carlo simulations are employed to assess bias and variability of the binding macroparameters (K_i and λk_3) as a function of the voxel noise level and the range of basis functions. The results show that for a [11C]CURB time activity curve with noise levels corresponding to a voxel of an image acquired with the HRRT and reconstructed with the filtered back projection algorithm, the implementation of BAFPIC requires the use of a constant vascular fraction of tissue (5%) and a cutoff for slow frequencies (0.06 min^{-1}). With these settings, BAFPIC maintains the probabilistic distributions of the binding macroparameters with approximately Gaussian shape and minimizes the bias and variability for large physiological ranges of the rate constants of [11C]CURB. BAFPIC reduces the variability of K_i to a third of that given by Patlak plot, the standard graphical method for irreversible radioligands. Application to real data demonstrated an excellent correlation between region of interest and BAFPIC parametric data and agreed with the simulations results. Therefore, BAFPIC with a constant vascular fraction can be used to generate parametric maps of [11C]CURB images acquired with an HRRT provided that the limits of the basis functions are carefully selected.

Introduction

Fatty acid amide hydrolase (FAAH, EC3.5.1.99) is the major metabolizing enzyme responsible for terminating the action of the endocannabinoid anandamide (N-arachidonoylethanolamide, AEA) and other fatty acid amides (e.g., oleoylethanolamide (OEA) and palmitoylethanolamide (PEA)). As such, FAAH sets the tone for endocannabinoid signaling and therefore

modulates what is believed to be a range of human behaviors and processes including motor, pain, inflammation, pregnancy, appetite, mood, cognition, and addiction. We recently developed and evaluated [^{11}C-carbonyl]URB694 ([^{11}C]CURB) for positron emission tomography (PET) quantification of FAAH binding in the human brain[1, 2]. Using a region of interest (ROI) analysis and an arterial plasma input function, we found that the irreversible 2-tissue compartment model (2-TCMi) provided an accurate fitting of the time activity curves (TAC). Additionally, the net influx constant K_i and the composite parameter λk_3 with $\lambda = V_{ND} = K_1/k_2$ had a coefficient of variation (*CoV*) less than 5% with 60 minutes of scan data and the uptake of [^{11}C]CURB was far from being flow-limited ($k_3/k_2 \sim 0.55$) [3]. Using PF-04457845[4, 5], a highly specific FAAH inhibitor, we confirmed that the first compartment of the 2-TCMi represents free and non-specific binding[2].

While the ROI level analysis is the preferred method when the anatomical localization of the areas of interest can be hypothesized, the voxel level analysis maximizes the potential of exploratory and/or data driven analyses. However, voxel level quantification is challenging as a result of the inherent noisy data. Due to the computational demands and numerical deficiencies to converge to the global minimum, non linear fittings of compartmental models are not usually a viable option for the creation of parametric maps (i.e. images containing the kinetic parameter value for each voxel) and as a result several approaches have been developed [6]. The classical methods are based on linearization of the kinetic equations (i.e. graphical analysis), which strongly reduces the computational demands. The most widely used method for irreversible radioligands with an input function is the Patlak plot[7]. This method does not assume a number of reversible compartment; however, it requires that the slowest reversible compartment is in effective equilibrium with the tracer in plasma[8], otherwise the estimation of the net uptake constant (K_i) will be biased. At the high noise level of a small voxel's TAC, the Patlak plot produces unacceptable variability for the images studied here (see results), demonstrating the need for an alternative method. Basis function methods (BFM)[9–11] allow for the linearization of the kinetic model equations using a family of basis functions. BFMs are known for reducing the variability of the parameter estimations. The application of BFMs, for an irreversible two-tissue compartment model with arterial input function, was recently introduced as BAFPIC[12]. While the outcome of Patlak plot is limited to K_i, BAFPIC can produce estimations of the individual rate constants. The members of the basis function family are the convolution of monoexpontial functions of different decay time constants (sometimes referred to as "frequencies") with the arterial input function. BFMs can be seen as a specific case of spectral analysis[13] in which the number of monoexponential convolutions to model a radioligand is known (e.g. radioligands, whose kinetics are described by the 2-TCMi, will activate only a single frequency of the frequency spectrum when analyzed with spectral analysis[14]). . Low frequency exponentials in spectral methods are known to produce biases in the estimation of the parameters[15]. This bias, however, has not been studied for BAFPIC, in which the frequencies (θ) have a simple expression as function of the rate constants ($\theta = k_2 + k_3$).

The goal of the present work is to validate the generation of parametric maps of [^{11}C]CURB using BAFPIC with images acquired on a high resolution research tomograph (HRRT, CPS/ Siemens, Knoxville, TN, USA). The small crystal dimension in the HRRT tomograph results in improved spatial resolution, though with a concomitant reduction in the reconstructed voxel signal to noise. This reduction in voxel signal to noise is the direct consequence of the crystal dimension which defines the sinogram sampling distance. A smaller voxel size, additionally, allows a more precise description of the anatomical structure. Hence it is both, an excellent and challenging tool to investigate radioligand binding at the voxel level.

In this work, we first determined the optimal setting for BAFPIC using simulations and later, using experimental human data, we validated the predictions of the model. The shape of

the probability distribution, bias and variability of K_i, λk_3 and the fractional blood volume (V_B) were studied using computer simulations which included: TACs with multiple sets of realistic combinations of the rate constants values, TACs with different noise levels, basis function with different ranges and numbers, and the use of V_B as a constant or as a variable. Results were compared with those from Patlak plot. Finally, the simulated results were confronted with real data. A comparison between region of interest analysis and voxel by voxel analysis was performed using a Bland-Altman plot for 6 healthy subjects at baseline and in the blocked condition using the FAAH inhibitor, PF-04457845. The expected performance of BAFPIC predicted by the simulations are presented as a function of voxel noise level and FAAH concentrations; therefore, the results of the work can immediately be applied to images of [^{11}C]CURB obtained with other scanners, algorithms of reconstruction or denoising filters post-reconstruction.

Material and methods

Kinetic analysis

Following the definitions proposed in the consensus nomenclature for radioligands[16], the TAC $C_T(t)$ of a radioligand described by an irreversible 2TCM with metabolites-corrected arterial input function $C_a(t)$ and radioactivity in the vascularity $C_b(t)$ can be described as [17]:

$$C_T(t) = \frac{(1 - V_B)}{\theta} K_1 k_3 \int_0^t C_a(\tau)d\tau + \frac{(1 - V_B)}{\theta} K_1 k_2 e^{-\theta t} \otimes C_a(t) + V_B C_b(t) \tag{1}$$

Where

$$\theta = k_2 + k_3 \tag{2}$$

Using a family of basis functions (BF$_j$, $j = 1..n$) of n exponential convolution of the input function:

$$BF_j(t) = e^{-\theta_j t} \otimes C_a(t) \tag{3}$$

with θ_j logarithmically spaced in the range [θ_{min}, θ_{max}][11, 18], Eq 1 can be converted in n linear equations of the shape:

$$\begin{bmatrix} \phi_1 \\ \phi_2 \\ V_b \end{bmatrix} = A_j^{-1} W C_T \tag{4}$$

Where $A_j = W[\int C_a(t) \, BF_j(t) \, C_b(t)]$, $\phi_1 = (1-V_B)K_1 k_3/\theta$, $\phi_2 = (1-V_B)K_1 k_2/\theta$ and W is a diagonal matrix of weight of the data points. A_j^{-1} can be computed using QR decomposition.

The linear equation for the value θ_j that minimizes the weighted residual sum of squares is chosen as the optimal solution. The rate constants can be computed as:

$$K_1 = (\phi_1 + \phi_2)/(1 - V_B), \; k_2 = \phi_2\theta/(\phi_1 + \phi_2), \; k_3 = \phi_1\theta/(\phi_1 + \phi_2) \text{ and } K_i = \phi_1/(1 - V_B)$$

Eventually, V_B can be assumed as a constant rather than a variable, and thus the vascular contribution can be subtracted from the TAC prior to solving the equation. In this case, $A_j = W[\int C_a(t) \, BF_j]$ and we will merely have two variables (ϕ_1 and ϕ_2). While in a large gray matter region, which is composed of a mixture of capillaries and brain tissue, it is expected that $V_B \sim 5\%$, this simplification is conflictive at a voxel level as it can be entirely inside of an artery ($V_B = 100\%$).

K_i of irreversible radioligands is usually estimated with the Patlak plot[7]. K_i^{Patlak} corresponds to the slope of the plot $C_T(t)/C_a(t)$ vs $\int C_a(t)/C_a(t)$ after a time t* in which it reaches

linearity. It takes place after all the reversible compartments in the system have reached effective equilibrium with the plasma compartment[8]. Patlak plot is usually applied subtracting a vascular contribution with a given V_B^{Patlak} from the TAC. Our previous ROI analysis of [^{11}C]CURB showed that the Patlak plot underestimates the K_i value given by the 2TCMi [1]. In the present work, Patlak plot was applied after correcting the TAC for a 5% of vascular contribution.

Simulations

Rate constants for TAC. Monte Carlo simulations were performed to assess 1) the shape of the distribution, bias and variability of K_i, λk_3 and V_B as a function of noise and range [θ_{min}, θ_{max}], 2) bias and variability introduced by fixing V_B to an incorrect value. Patlak plot was also performed for comparison.

The main simulations used in this work were based on the 60 minutes decay corrected TAC created by the rate constant of an average "putamen" (K_1^P = 0.31 mL·cm^{-3}·min^{-1}, k_2^P = 0.1 min^{-1} and k_3^P = 0.049 min^{-1})[1].

Changes in regional cerebral blood flow (rCBF) were simulated by changing K_1. Our previous results[1] led to a very low rCBF (~20 mL·100 mg^{-1}·min^{-1}) with K_1 = 0.16 mL·cm^{-3}·min^{-1} and a very high rCBF (~110 mL·100 mg^{-1}·min^{-1}) with K_1 = 0.36 mL·cm^{-3}·min^{-1}. Changes in V_{ND} were simulated by changing k_2 for a given K_1 value. Previous results showed that V_{ND} is within the range 2 to 4 mL·cm^{-3}. Additional simulations were performed with combination of those maximum and minimum rCBF and V_{ND} values and with typical rCBF (K_1 = 0.31 mL·cm^{-3}·min^{-1}) and very high V_{ND} = 4.5 mL·cm^{-3}.

Changes in B_{max} (FAAH activity) were modeled by multiplying k_3^P by 0.1, 0.2, 0.35, 0.5, 0.75, 1, 1.25, 1.5 and 2.

The same arterial unmetabolized radioligand in plasma (input function) and whole blood curve of a typical subject were used for all the simulations. In all simulations, V_B^{TAC} = 5% except in the simulation for examining the bias caused by fixing V_B to a wrong value in BAFPIC (V_B^{TAC} = 0%, 5%, 10% and 25%).

Setting for the basis functions (BFs): Range and number

Given that $\theta = k_2 + k_3$ and $k_3 = k_{on}B_{max}$, a BF with $\theta_{min} < k_2^{min}$ applied to Eq 1 should describe the TAC of a voxel without FAAH (k_3 = 0) and a BF with $\theta_{max} > k_2^{max} + k_3^{max}$ should describe the TAC of the maximum expected B_{max}. While θ_{min} = min (θ) will produce the BF that washes out slowest, θ_{max} = max(θ) will produce the quickest BF washing out (Fig 1).

From our ROI based analysis of [^{11}C]CURB, we have learned that by accounting for one standard deviation, k_2^{min} = 0.07 min^{-1} (caudate), k_2^{max} = 0.13 min^{-1} (temporal ctx) and k_3^{max} = 0.067 min^{-1} (cerebellum)[1]. Therefore, the BF set explored in this work includes: θ_{min} = 0.01, 0.02, 0.03, 0.04, 0.05, 0.06 and 0.07 min^{-1} and θ_{max} = 0.2, 0.5, 1 2, 3 min^{-1}. We studied BF with n = 50, 100 250, 500 and 1000 member logarithmically separated between θ_{min} and θ_{max}.

For clarity, in the rest of the manuscript, the BF will be described as n = 50 *frequencies* logarithmically spaced between [θ_{min}, θ_{max}]

Noise and weight for fittings

Noise for the frame i from time t_i^s to t_i^e was modeled with a Gaussian distribution with standard deviation (SD_i):[19]

$$SD_i = sf \sqrt{\frac{e^{\lambda_c(t_i^e + t_i^s)/2}C_i}{(t_i^e - t_i^s)}}$$
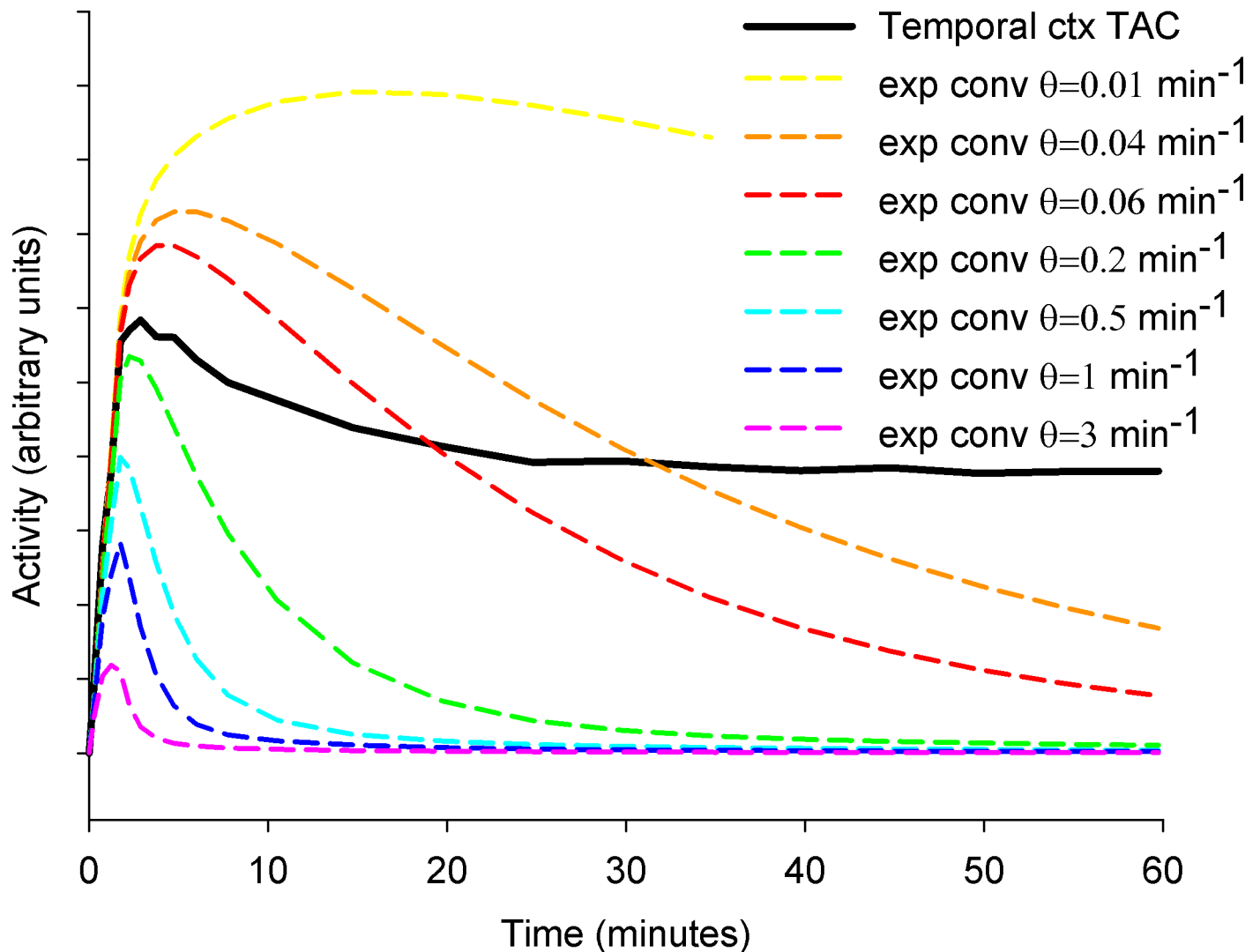
(5)

Fig 1. Exponential convolution of the input function of a single subject for different time constant θ compared with a regional TAC (temporal ctx) for the same subject. The TAC's peakwidth is mostly given by a single basis function. Taking into account different regional TACs, it gives an idea about the set of elements to include in the basis.

where C_i is the noise-free simulated radioactivity, λ_c = 0.0339 min^{-1} is the decay constant of ^{11}C and *sf* is the scale factor that controls the noise level. The mean percent noise contained in the noisy data was calculated as[20]: $\%\Sigma_i SD_i/\Sigma_i C_i$. *sf* = 7 is characteristic of noise in a typical sized ROI, *sf* = 20 of a very small ROI (i.e. anterior cingulate cortex) and *sf* = 100~120 of a single voxel in the gray matter of an image acquired and reconstructed as previously published[1, 2] (i.e acquired by an HRRT following a bolus injection with 10 mCi of [^{11}C]CURB and reconstruction using the 2D filtered-back projection (FBP) algorithm, with a HANN filter at Nyquist cutoff frequency. For details see [1]). The Coefficient of variation (*CoV*) reported in the simulation was calculated as the standard deviation/mean.

Human studies

The human analysis presented here is a parametric maps analysis of a study previously published using a region of interest (ROI) approach[2]. The protocol was approved by the Center

for Addiction and Mental Health Ethics Review Board and conformed to the Declaration of Helsinki. All subjects provided written informed consent after all study procedures were fully explained. Images of six healthy volunteers (3 men and 3 women; aged 19–53 years) were acquired before and 2 hours after an oral dose of a potent specific FAAH blocker, PF-04457845. A saline solution of 370 ± 40 MBq (10± 1 mCi) of [11C]CURB was injected over a 1-minute period at a constant rate using a Harvard infusion pump (Harvard Apparatus, Holliston, MA, USA) into an intravenous line placed in an antecubital vein. The images were reconstructed into 22 time frames. The first frame was of variable length dependent on the time between the start of acquisition and the arrival of [11C]CURB in the tomograph field of view (FOV). The subsequent frames were defined as 5x30 sec, 1x45 sec, 2x60 sec, 1x90 sec, 1x120 sec, 1x210 sec and 10x300 sec. All images were decay corrected. The arterial blood analysis, input function creation and delay and dispersion calculation were previously described[1, 2]. Results of the blocking study in the white matter (WM) were not previously explored. WM delineation was performed following the algorithm described in Bencherif et al.[21], which includes WM predominately from the corpus callosum, allowing for a maximum of 5% partial volume effect from the gray matter. Head movement in the dynamic PET acquisition was corrected using a frame-by-frame realignment of images reconstructed iteratively unweighted OSEM (3 iterations, subset 6, span 3) without attenuation correction[22]. TACs were fitted assuming V_B = 5% [23] and data point weighted based on the trues in the field of view[24].

Results

Simulations

Fig 1 shows the $BF_j(t)$ for a typical input function and a set of values θ_j. The position of the peak of $BF_j(t)$ increases when θ_j decreases.

Considering Fig 1 and Eq 1, the position and width of the peak of the TAC of [11C]CURB is given mainly by $BF_j(t)$. Therefore, comparing the position of the peak of BFs respect to the TAC can help to verify whether the range [θ_{min}, θ_{max}] is reasonable. Typical TACs for [11C]CURB show a peak between 120 to 260 seconds after injection[1]. For $\theta \geq 0.2$ min^{-1} the peak, before 180 sec after injection, will be too early for some regional TACs. For $\theta \leq 0.02$ min^{-1} the peak will be too late (after 500 seconds). Thus, θ = [0.06, 0.2] min^{-1} represents a conservative initial estimation for the range of θ for a TAC of [11C]CURB in a gray matter region of a healthy subject.

Results of the simulations are reported in a Microsoft Office Excel file (S1 File).

Number of simulations

The percentage error of the mean (E) in n_c Monte Carlo simulations for a given confidence interval with critical value z_c can be estimated as $E = \frac{100 z_c S_x}{\bar{x} \sqrt{n_c}}$, where $\bar{x}$ and S_x are the sample mean and sample standard deviation for a large number of simulations. As it will be seen below, $\bar{x}$ and S_x were highly dependent on the data simulated, the noise level and the model used for quantification. The results presented in this work have been calculated using n_c = 5000, which using a confidence level of 95% (z_c = 1.96) led to $E \ll 5\%$ in most of the scenarios studied. Exceptions occurred in cases with a very low $\bar{x}$ and a very high S_x, which have been observed using BAFPIC with a low θ_{min} (0.01 min^{-1}) or Patlak model on data with high levels of noise (sf = 120) and low specific binding (k_3/k_3^P = 0.1 or 0.2).

Simulation results using BAFPIC with constant VB = 5%

Minimal basis set. Basis set including n = 2,3,4,5,10,25,50,100,250,500 and 5000 members were evaluated in the largest range of θ = [0.01, 3] min^{-1} studied and the optimal range of θ =

[0.06, 3] min^{-1} (see below). At any noise level $sf>7$, $n>50$ does not produce further evolution in the probability distribution of K_i and λk_3 (regarding mean, standard deviation (std), kurtosis ($kurt$) and skewness ($skew$)). Results presented in this manuscript were calculated using $n = 50$.

Interestingly, when the noise level decreases, more BFs are required. At $sf = 7$, a noise level of a middle sized ROI TAC (i.e putamen), $n = 100$ was required when the largest range [0.01, 3] min^{-1} was used. The discretization of θ becomes more inefficient for TACs with lower noise: the noise of the TAC induces variability in ϕ_1 and ϕ_2 but not in θ. Increasing n corrects this problem. For very low noise ($sf = 1$), when $n<500$, only two BFs with neighbor exponents are chosen and the distributions of rate constants presents more than one peak.

Probability distribution of K_i as a function of sf and $[\theta_{min}, \theta_{max}]$

A visual presentation of the bias and CoV of K_i and λk_3 is presented in Fig 2. For $sf = 20$, K_i showed a non-biased normal distribution (bias<1%,CoV~6%, $skew$ ~-0.3, $kurt$~3.1–3.5) practically independent of θ_{min} and θ_{max}.

At higher levels of noise, the variability of K_i progressively increases and an underestimation of K_i progressively appears. The distribution of probability of K_i, becomes a non Gaussian shape (negative $skew$ and $kurt>3$). This effect depends more strongly on θ_{min} than on θ_{max} (i.e more underestimation when slower frequencies of the BF are included, but the faster frequencies play a secondary role). Reasonable normal distributions (-1<$skew$<0, 3<kurt< = 4) can be seen for basis function ranges [0.04 < = θ_{min}< = 0.07, θ_{max}> = 0.2] min^{-1}. At these ranges, for a given noise level, bias and CoV increase nearly linearly when θ_{min} decreases and it is practically independent of θ_{max} (Fig 2A). [$\theta_{min}\geq0.06$, $\theta_{max} \geq1$] minimized the underestimation and CoV (e.g. for [0.06, 3] min^{-1} the bias is limited to -5.6% and CoV = 40% for the maximum noise studied ($sf = 120$)). On the other extreme, the worse scenario is for $\theta_{min} \leq0.02$ min^{-1} (e.g. for [0.02, 3] min^{-1} the underestimation was quadruple and CoV double compared to [0.06, 3] min^{-1}).

Probability distribution of λk_3 as a function of sf and $[\theta_{min}, \theta_{max}]$

At $sf = 20$, the noise level of a TAC of a very small ROI, λk_3 shows a normal distribution without bias and CoV~10% at any BF range.

For $sf\geq40$, λk_3 distributions showed a high kurtosis (e.g. 4$\leq kurt\leq$ 8 for $sf = 40$, 8$\leq kurt\leq$ 145 for $sf = 60$) and for $sf>60$ the distribution showed a high skewness as well.

Similar to the case of K_i, λk_3 bias depends more strongly on the selection of θ_{min} than θ_{max}. Bias (underestimation) can be reduced by selecting the range of θ (higher θ_{min} and lower θ_{max}); however, the COV follows the opposite trend (e.g at higher noise ($sf = 120$) for $\theta = [0.06, 3]$ min^{-1}, the bias = -15% and $CoV = 77\%$ and for $\theta = [0.06, 0.2]$ min^{-1}, bias = -12% and CoV = 103%). It should be noted that, at the same noise level, even a "low" CoV for λk_3 is higher than a typical CoV for K_i (Fig 3, Fig 2B vs Fig 2D).

Effects of V_B fixed to a wrong value on the probability distribution of K_i

In the previous section, we fixed $V_B = 5\%$ and $V_B^{TAC} = 5\%$. In the present section, K_i distributions were analyzed when TACs were simulated with $V_B^{TAC} = 0\%$, 5%, 10% and 25% and BAFPIC was implemented with $V_B = 5\%$. Simulations were done at high noise levels ($sf = 100$ and 120) and BAFPIC using [0.06, 3] min^{-1}.

The result (S1 File, sheet "VB") demonstrated that an error of X = $V_B^{TAC} - V_B$ percentage points in V_B will induce an extra bias in K_i of approximately -X%. Interestingly, for $V_B^{TAC} = 0$,
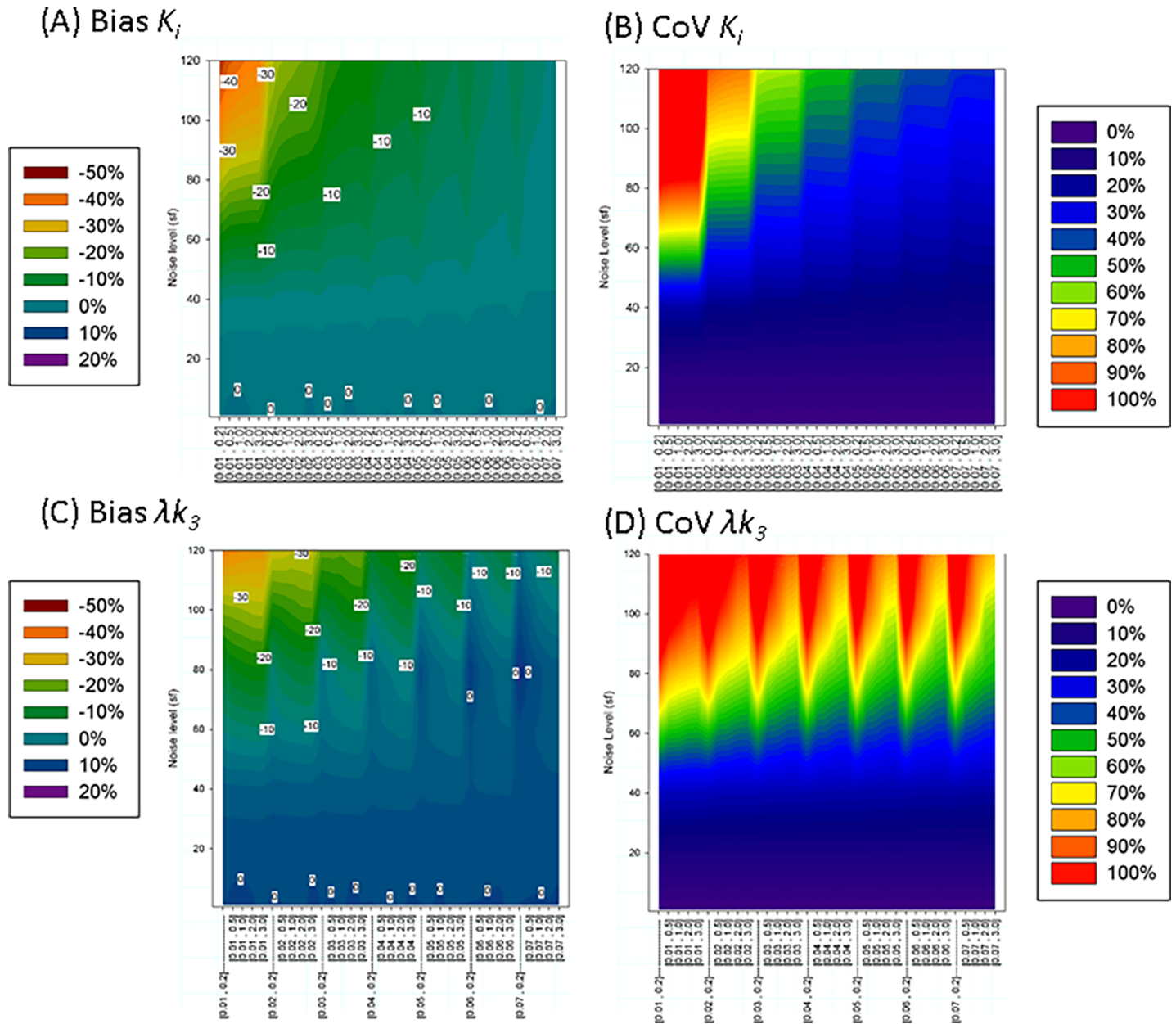
Fig 2. Visual representation of the simulated results using BAFPIC with Vb≡5%. Each vertical line represent the effect of noise in the bias and coefficient of variation (CoV) for a given range [θ_{min}, θ_{max}] of the basis functions. Noise is expressed as the value of the scale factor in Eq 5. Results show that bias and CoV depend more on θ_{min} than θ_{max}.

https://doi.org/10.1371/journal.pone.0192410.g002

(X = -5), the noise-induced underestimation will cancel out the overestimation due to the error in the V_B.

Probability distribution of K_i and λk_3 for different Bmax

In this section, BAFPIC with V_B = 5% and θ = [0.06, 3] min⁻¹ and θ = [0.07, 3] min⁻¹ was used on simulated highly noisy TACs (sf = 120). k_3 was changed to model different FAAH activities; k_3/k_3^P = 0.1, 0.2, 0.35, 0.5, 0.75, 1, 1.25, 1.5 and 2 were studied. At higher values of k_3, the irreversible radioligand start to show delivery limitation effects.
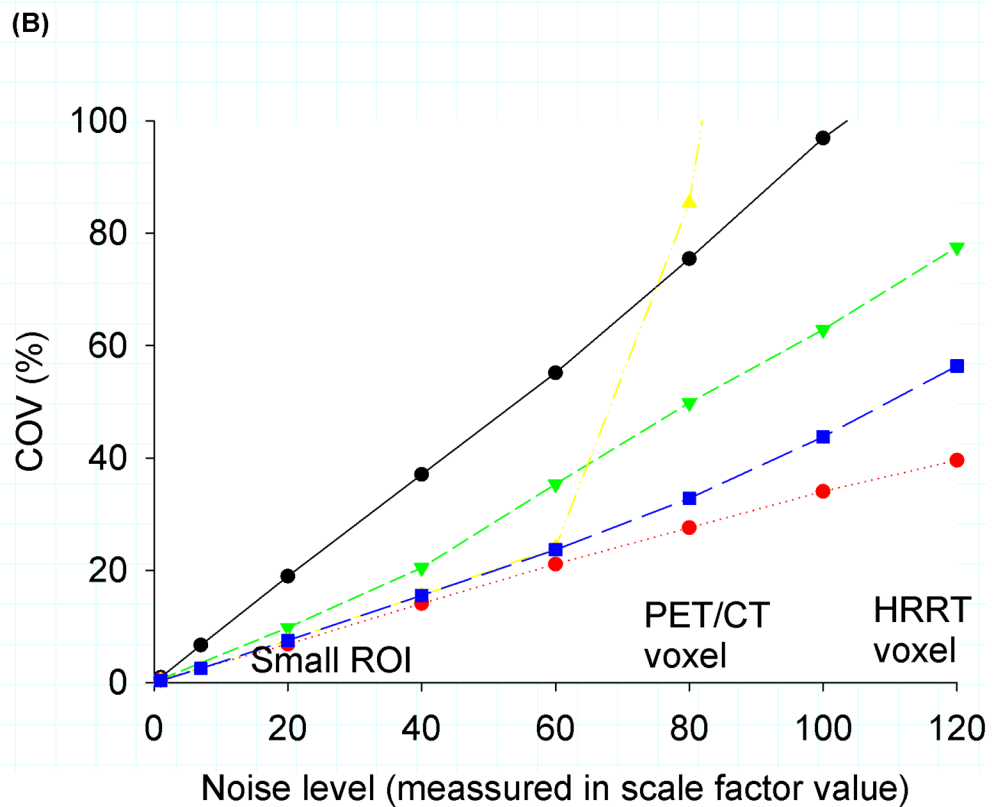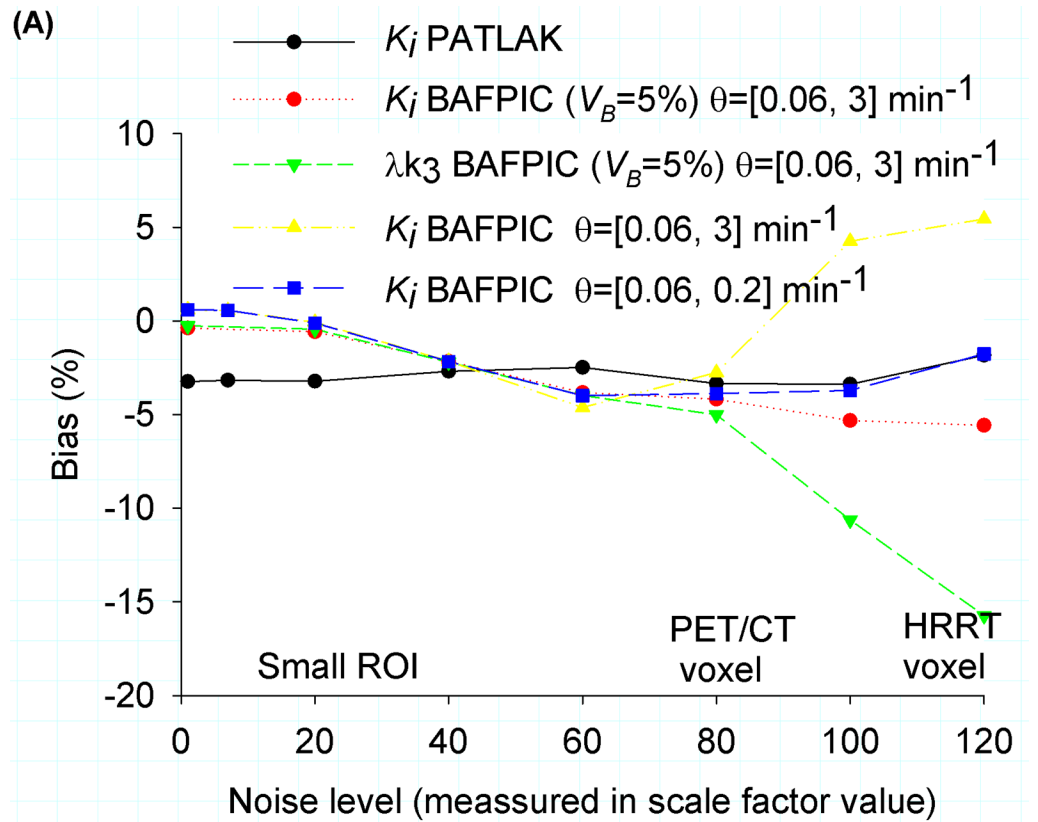
(A)

(B)

Fig 3. Bias = (mean(K_i simulation)/K_i simulated-1)% and CoV = std(K_i simulations)/mean(K_i simulation) as a function of the noise level ([Eq 5](#)). As a reference, we included the approximate voxel noise level of a PET/CT camera (Biograph HiRez XVI. Siemens Molecular Imaging) and a HRRT (CPS/Siemens, Knoxville, TN, USA).

Results showed that K_i presents a relative bias that depends on the value of K_i and the BF range ([Fig 4](#), green and yellow lines). For $\theta = [0.06, 3]$ min^{-1}, when k_3 is in the range $0.35 < k_3/k_3^p < 2$, K_i bias changes from ~-10% to ~-4%. But when $k_3/k_3^p < 0.35$, corresponding to the cases when the noisy TAC can be fitted equally well by a 1TCM and 2TCMi, the K_i bias and CoV become more pronounced ([Fig 4](#) yellow line). In contrast for $\theta = [0.07, 3]$ min^{-1}, the underestimation of K_i is lessened and bound within 10% for any k_3 ([Fig 4](#), green line). It should
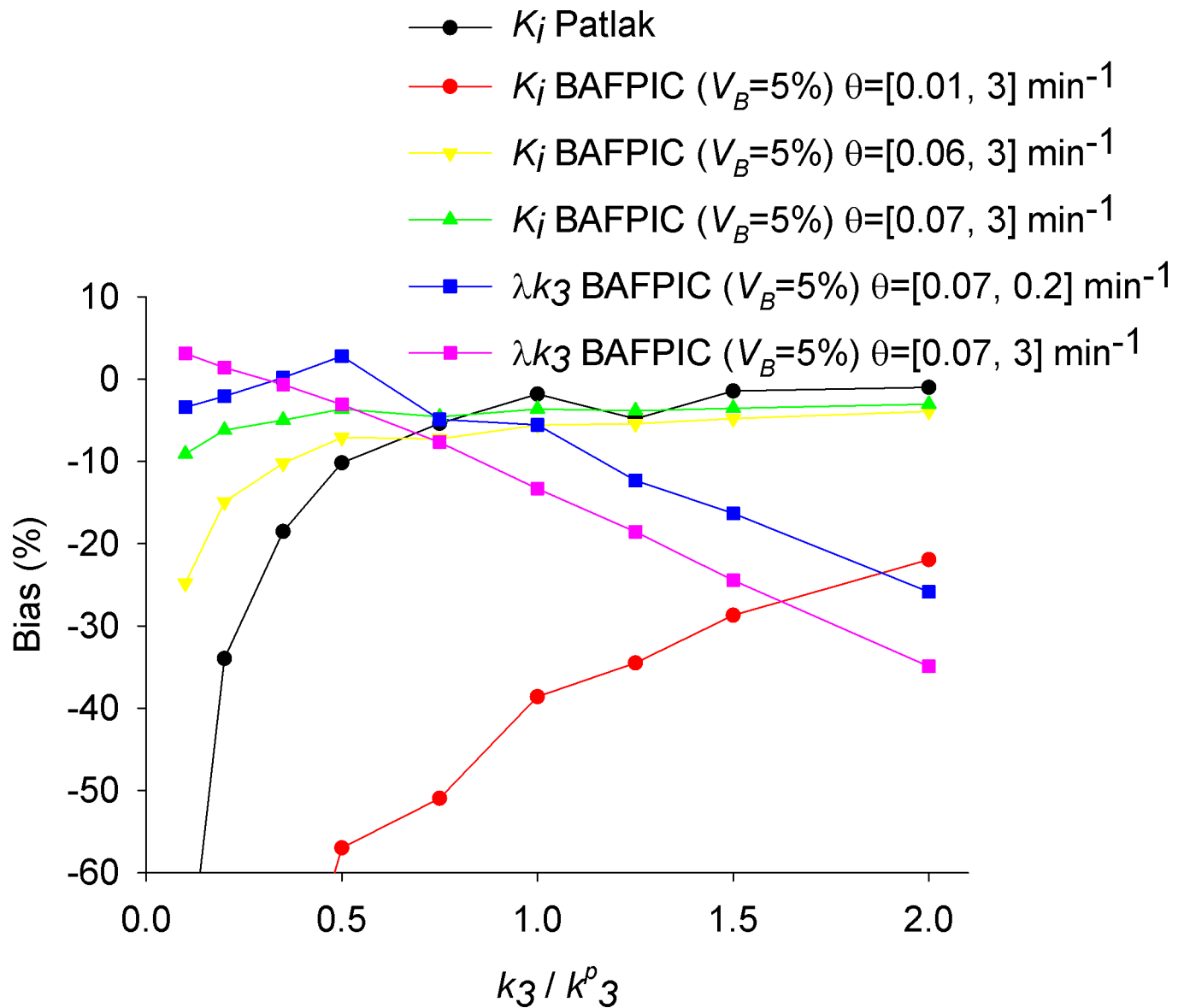

Fig 4. Noise induced bias for K_i and λk_3 estimated by BAFPIC and for K_i estimated by Patlak plot as function of k_3/k_3^p. The simulated noise corresponds to TACs that are regularly observed at the HRRT voxel level ($sf = 120$). Bias is computed as ((measured-simulated)/simulated)%. Note that the yellow line in this figure corresponds to the yellow line in [Fig 5](#).

be noted that the use of relative bias (%) and CoV can be misleading for small k_3 values, and actually the absolute bias and standard deviation present the opposite trend (S1, S2 and S3 Figs).

λk_3 presented a more complex and varied pattern of bias under k_3 changes and the θ range used (Fig 4, blue and purple lines). Importantly, the bias is bound within ±5% for small changes around k_3^P (e.g. λk_3 bias increases from ~-8% to ~-19% when k_3/k_3^P increases from 0.75 to 1.25 using θ = [0.07, 3] min^{-1} and the direction of change is such that a simulated reduction of ~40% would be measured by BAFPIC as attenuated to ~32%). CoV(λk_3) presented a minimum >67% for k_3/k_3^P~0.5 (S1 Fig).

Probability distribution of K_i for low and high rCBF and V_{ND} values as a function of B_{max}

These simulations were only performed for V_B = 5%, V_B^{TAC} = 5%, noise level sf = 120, and BF with θ = [0.06, 3] min^{-1}. The distribution shape of K_i is reasonably Gaussian, based on kurtosis and skewness. A systematic bias of K_i as a function of a simulated K_i value is observed in the continuous lines of Fig 5. At high k_3 values, all the simulations underestimated K_i. At a low k_3, the underestimation of K_i was lower (Fig 5, blue, green and red lines) or in some cases there
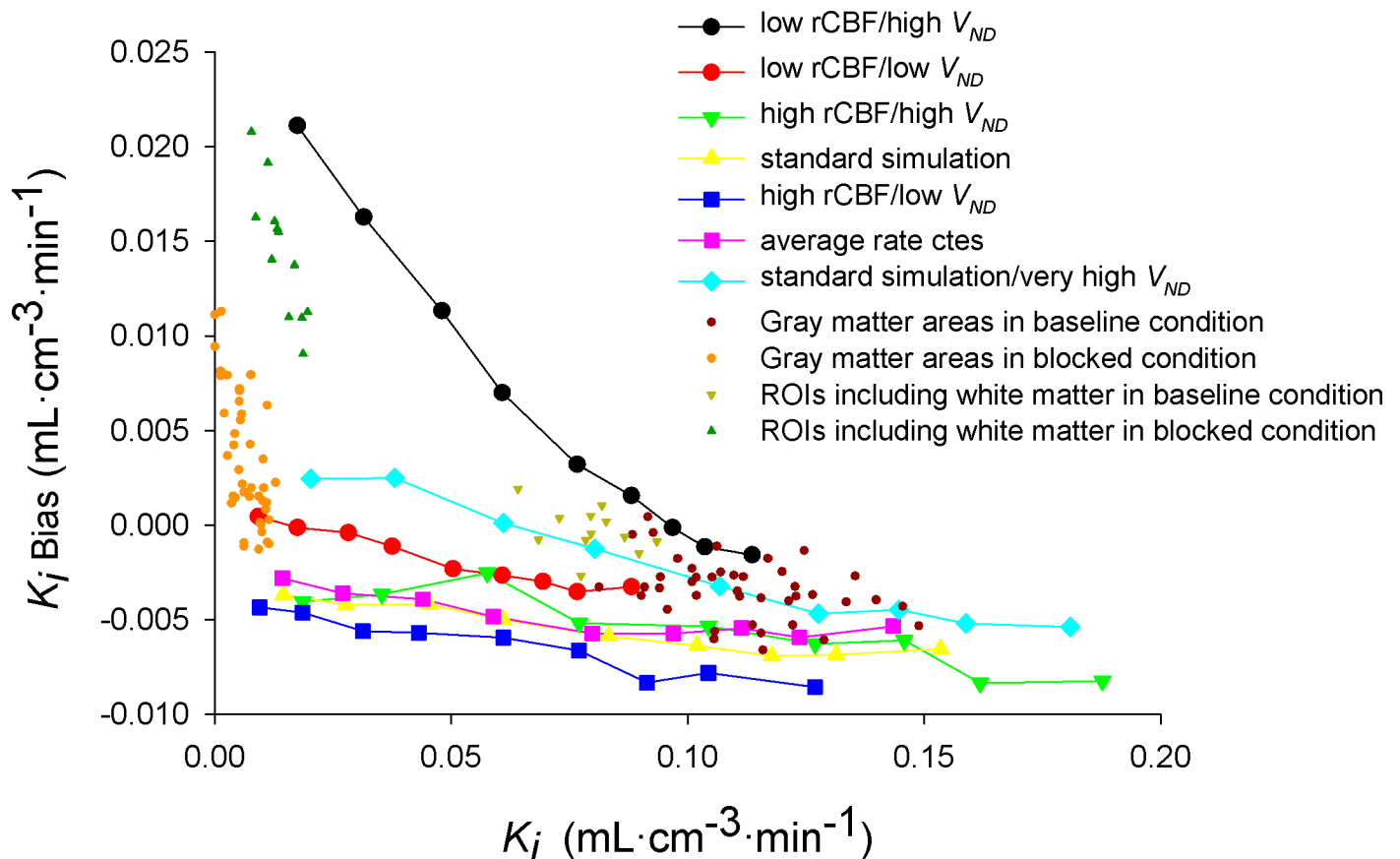

Fig 5. Bias as a function of K_i. The simulated results are represented by the solid symbols connected with lines. In these cases, the x-axis represents the simulated K_i value while the y-axis is the mean K_i of the simulation minus the simulated value. Symbols along the line are simulations with the same K_1 and V_{ND} but a different k_3. K_1 = 0.16 mL·cm^{-3}·min^{-1} (Low rCBF), K_1 = 0.36 mL·cm^{-3}·min^{-1} (high rCBF), V_{ND} = 2, 4 and 4.5 mL·cm^{-3}(Low, High, very high respectively). Scattered points are data from real images (6 subjects/9 ROIs/2 scans per subject). In these cases, K_i in the x-axis is the result of the 2TCMi on the regional TAC while the y-axis is the regional mean of K_i in the BAFPIC based parametric map minus the regional 2TCMi estimation. BAFPIC was applied with 50 function with θ in the range [0.06 3] min^{-1} and V_B = 5%.

was an overestimation (Fig 5, cyan and black lines). Bias values depend on the simulated rCBF and V_{ND}. While for most of the simulations the bias was limited to *circa* ±5% of the baseline $K_{i(k_3/k_3^P=1)}$, a particularly marked overestimation was observed for the case of low rCBF/High V_{ND} (Fig 5, black line, K_I = 0.16 mL/cm^3/min, k_2 = 0.04 min^{-1}) when k_3 is low as a consequence of θ_{min} = 0.06 min^{-1} > k_2+k_3.

Simulation results using BAFPIC with V_B variable

Fig 6 represents the summarized result of the simulations.

Probability distribution of V_B as a function of *sf* and [θ_{min}, θ_{max}]

Members of the basis function with higher frequencies look more similar to the input function (Fig 1). High frequencies are related to the rapid transit time of the tracer in the vasculature within the ROI and effects of dispersion in the arterial line [13]. In presence of noise (sf>40), the mean value of V_B is practically determined by θ_{max} (Fig 6E) and θ_{max} between 0.2 min^{-1} and 0.5 min^{-1} keeps V_B closer to 5% (minimized the bias). Independent of the range of the basis, V_B presents a Gaussian distribution with high variability (for the optimal θ range for each sf, *CoV* increases from ~140% at *sf* = 40 to *CoV*~400% at *sf* = 120) (Fig 6D).

Probability distribution of K_i as a function of *sf* and [θ_{min}, θ_{max}]

At noise levels of a typical ROI (*sf* = 7) or even of a tiny ROI (*sf* = 20), K_i shows a normal distribution with low bias (<1%) and *CoV* = 2.5% and 7.5 for *sf* = 7 and *sf* = 20, respectively (Fig 6A and 6B, Fig 3A yellow and blue lines). For higher noise levels (*sf*≥40), the shape of the distribution (kurtosis and skewness) depends strongly on the range of θ considered. The distributions are leptokurtic (*kurt* >3). The kurtosis goes to 3 for higher θ_{min}. The bias of the mean is always negative (underestimation) and becomes stronger for higher θ_{max}. The *CoV* (and skewness) presents a minimum in the range 0.2< θ_{max} <1 for each *sf* and θ_{min}. θ = [0.06, 0.2] min^{-1} presents a good trade off, keeping a distribution shape closer to the normal and reducing bias and *CoV* (eg. for *sf* = 100, bias = -3.7%, *CoV* = 43%, kurt = 7, *skew* = 1.1)

While *CoV*(K_i) increases linearly with the noise level when applying BAFPIC with a fixed V_B (Fig 3B, red line), it increases exponentially when V_B is variable, using the optimal BF sets for each case (Fig 3B, blue line). For *sf*< = 60, the difference is not important, but for *sf* = 120, *CoV*(K_i) ≈40% using V_B constant vs *CoV*(K_i) ≈56% using V_B variable.

Probability distribution of λk_3 as a function of *sf* and [θ_{min}, θ_{max}]

BAFPIC estimations for λk_3 when V_B is variable were similar to those when V_B is constant, but with higher *CoV*s (Fig 6C and 6D). At *sf* = 20, λk_3 shows a normal distribution without bias and *CoV*~11% for any base function considered. For *sf*≥40, λk_3 distributions showed a high kurtosis (8≤*kurt*≤11 for *sf* = 40, 17≤*kurt*≤ 300 for *sf* = 60 and higher for higher noise). For *sf*≥60, the distribution presents a high skewness as well. For sf>60, the variability is so large (*CoV*>67%) that the precise bias (usually underestimation) is difficult to determine. The bias depends more strongly on the selection of θ_{min} than θ_{max}; higher θ_{min} decreases the underestimation. For each θ_{min}, *CoV* is minimized for a θ_{max} between 0.5≤ θ_{max} ≤ 2 min^{-1} (e.g. for *sf* = 120 and θ = [0.06, 0.5], min^{-1} the bias is -11% and CoV = 126%.

Patlak plot as a function of *sf* and B_{max}

Patlak plot reached linearity for t* = 27.25 min in TACs with k_3/k_3^P = 1. Using this t*, K_i^{Patlak} showed a low underestimation (between -2% and -5%), practically independent of *sf*. The *CoV*
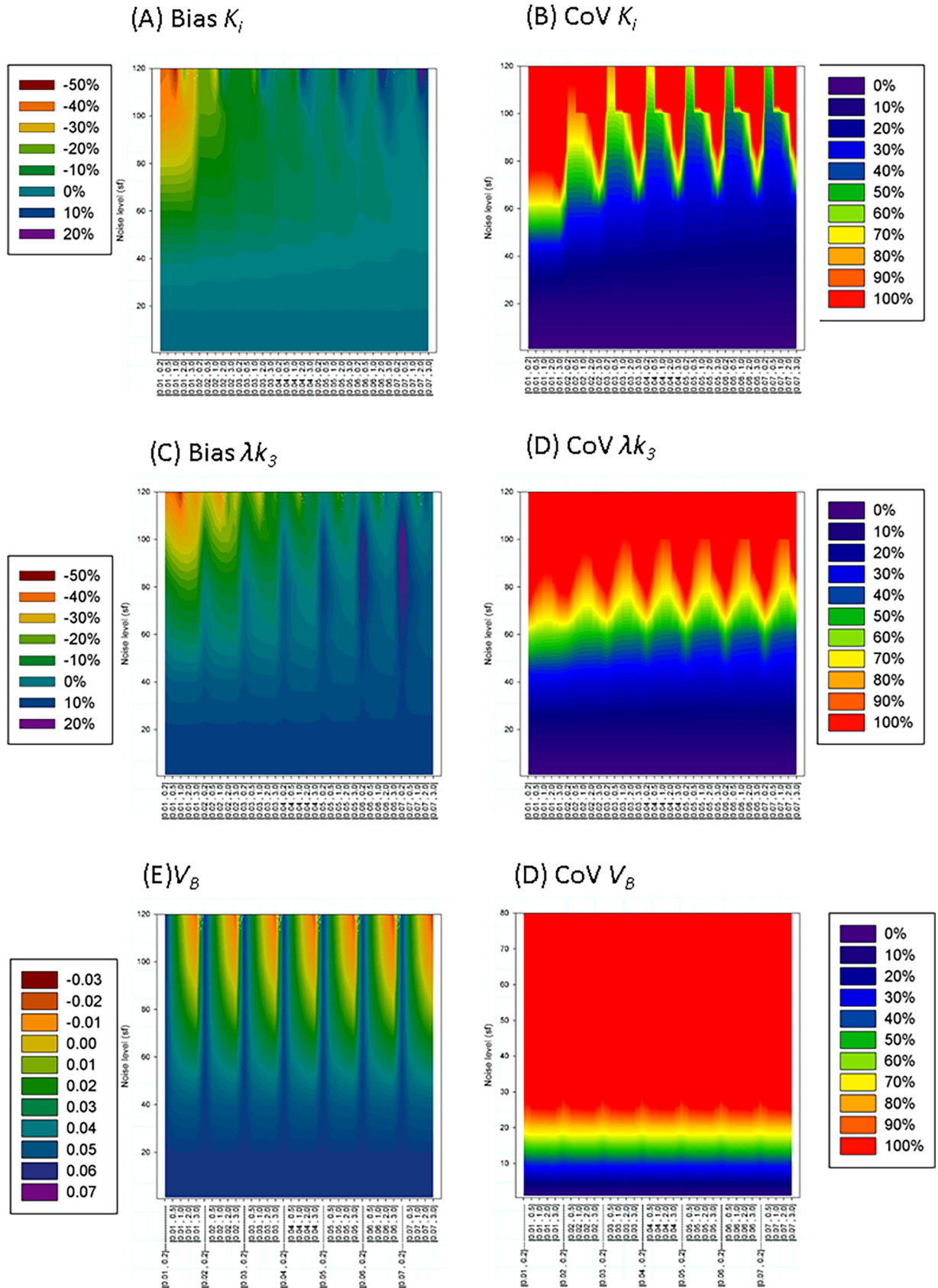
(A) Bias K_i

(B) CoV K_i

(C) Bias λk_3

(D) CoV λk_3

(E) V_B

(D) CoV V_B

of K_i^{Patlak} increased linearly with sf. CoV was more than 3 times higher than CoV of K_i with BAFPIC using a constant V_B (Fig 4, black vs red line). For $sf = 120$, the mean of K_i^{Patlak} was still fluctuating within ±2% after 5000 simulations.

At $sf = 120$, changes in k_3 did not induce a significant effect on the bias in the range of $0.5 \leq k_3/k_3^P \leq 2$ (Fig 4, black line). However, for $k_3/k_3^P < 0.5$, when the TAC can be fitted with 1TCM, a significant underestimation appeared reaching -76% for $k_3/k_3^P = 0.1$.

BAFPIC with constant V_B = 5%: Application to real images

Parametric maps were generated for 6 subjects in the baseline and block conditions using the optimal parameters found in the simulations ($\theta = [0.06, 3]$ min^{-1}, #*basis functions = 50*, Fig 7). Histograms of values inside the large homogeneous ROIs (e.g. cerebellum cortex, ~10^4 voxels) showed normal distributions (S4 Fig). Mean values in the parametric maps of each ROI correlated excellently with estimations given by the ROI analysis (r^2 = 0.992 including all ROIs in baseline and blocked conditions, and r^2 = 0.996 in the baseline condition only). Simulation-predicted bias as a function of K_i value was observed (Fig 5, color symbols). Overall the bias in Fig 5, including all ROIs data points, can be fitted by the linear regression: $\langle K_i^{par} \rangle - K_i^{ROI} = -0.092\ K_i^{ROI} + 0.0072$ min^{-1} mL·cm^{-3}·min^{-1} for $0 < K_i^{ROI} < 0.15$ mL·cm^{-3}·min^{-1}. However, this relationship is more complex than linear; in a blocked condition, regions containing white matter (Pons and Middle brain) showed a higher overestimation using BAFPIC than ROI, most likely due to $k_2 + k_3 < 0.06$ min^{-1}. On the other hand, it should be noted that in the blocked condition, the gray matter regions present a large dispersion in the bias without a clear pattern. The bias slightly decreases the differences measured in the parametric map (e.g. for a ROI with a K_i^{ROI} of 0.1 a change ±20% would be measured in the parametric maps as ±18.5%, a change of ±40% as ±37%, and a change of ±90% as ±83%). However, for a WM area, the linear relationship is not maintained (see Fig 5): a reduction of 83% from $K_i^{ROI} = 0.06$ to 0.01 would be measured in the parametric ~60% rather than the linear prediction of 73%. In summary, the bias would strongly depend on the relation of $k_2 + k_3$ with θ_{min}.

The bias found in the real data follows approximately the pattern predicted with the simulations. WM regions (low rCBF) fall in the middle of the simulations of low rCBF/high V_{ND} and low rCBF/low V_{ND}. However, gray matter ROIs behave as having a $V_{ND} = 4.5$ mL/mL, which is higher than reported in Rusjan *et al.* [1], yet closer to what was measured in blocking conditions in Boileau *et al* [2].

Previously, we have published in our gray matter ROI analysis a reduction of $\lambda k_3 > 90\%$ after 2 hours of an oral dose of ≥ 1 mg of PF-04457845[2]. It should be noted that while λk_3 is proportional to k_3, K_i is not directly proportional and is less sensitive to changes in k_3 depending on the ratio of k_3/k_2. A 90% reduction in k_3 should reduce K_i by 82% when $k_3 = k_2$ (e.g. gray matter) and 75% when $k_3 = 2k_2$ (e.g. white matter).

Fig 7 represents the average parametric K_i maps of the 6 subjects in the baseline and blocking conditions. In the gray matter, the reduction of K_i in the blocking condition is above 80%, which is consistent with our previously published result of a reduction of $\lambda k_3 > 90\%$. In contrast, the reduction in WM is merely ~40%, from $\langle K_i^{baseline} \rangle = 0.057$ mL·cm^{-3}·min^{-1} to $\langle K_i^{block} \rangle = 0.034$ mL·cm^{-3}·min^{-1}. These K_i values are within the range in which the bias behaves linearly and correspond to a reduction in k_3 of 45%-50%. In order to confirm these results, a
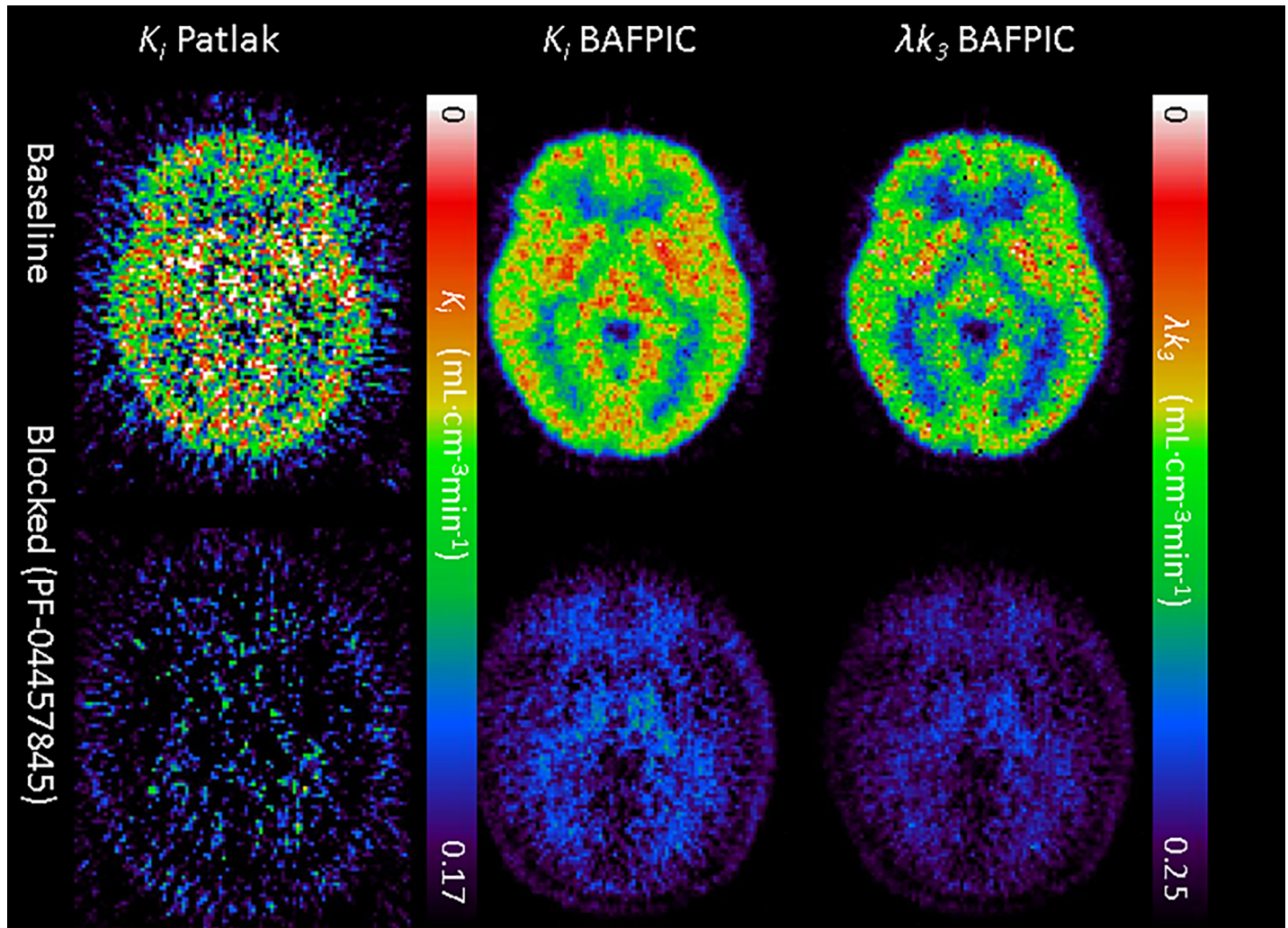
Fig 7. Axial slice (MNI z = +2mm) of the averaged (n = 6) parametric maps of K_i (Patlak and BAFPIC) and λk_3 (BAFPIC). The images in the upper row are at baseline condition, while the images on the lower row were acquired 2 hours after an oral dose ≥ 1 mg of PF-04457845. Note that while the gray matter changed substantially, the change is less marked in the white matter. Units are mL·cm^{-3}·min^{-1}.

large ROI of the WM was delineated (see methods) and the TAC was quantified using 2TCMi (Fig 8). While occupancy in gray matter was $>$ 95% and was practically dose-independent, the white matter presented a lower occupancy that was apparently dose dependent. Fig 7 shows that parametric maps of K_i estimated with Patlak or with λk_3 estimated with BAFPIC are more pixelated than K_i estimated by BAFPIC as a consequence of higher variability.

BAFPIC with variable V_B: Application to real images

Parametric maps using BAFPIC, with variable V_B, were consistent with the results of the simulations. BF with $\theta = [0.06, 0.2]$ min^{-1} provides realistic V_B values (~5%) with high variability. In contrast, the average parametric K_i values correlate weaker with the ROI estimation than when BAFPIC with a fixed V_B is used. Correlation of K_i becomes stronger for the BF with $\theta = [0.06, 0.5]$ min^{-1}, but estimations of V_B becomes too low to be considered realistic. V_B in the block condition is lower and more variable than in baseline. It should be remarked that V_B loses identifiability in the ROI analysis for the blocked TAC as well.
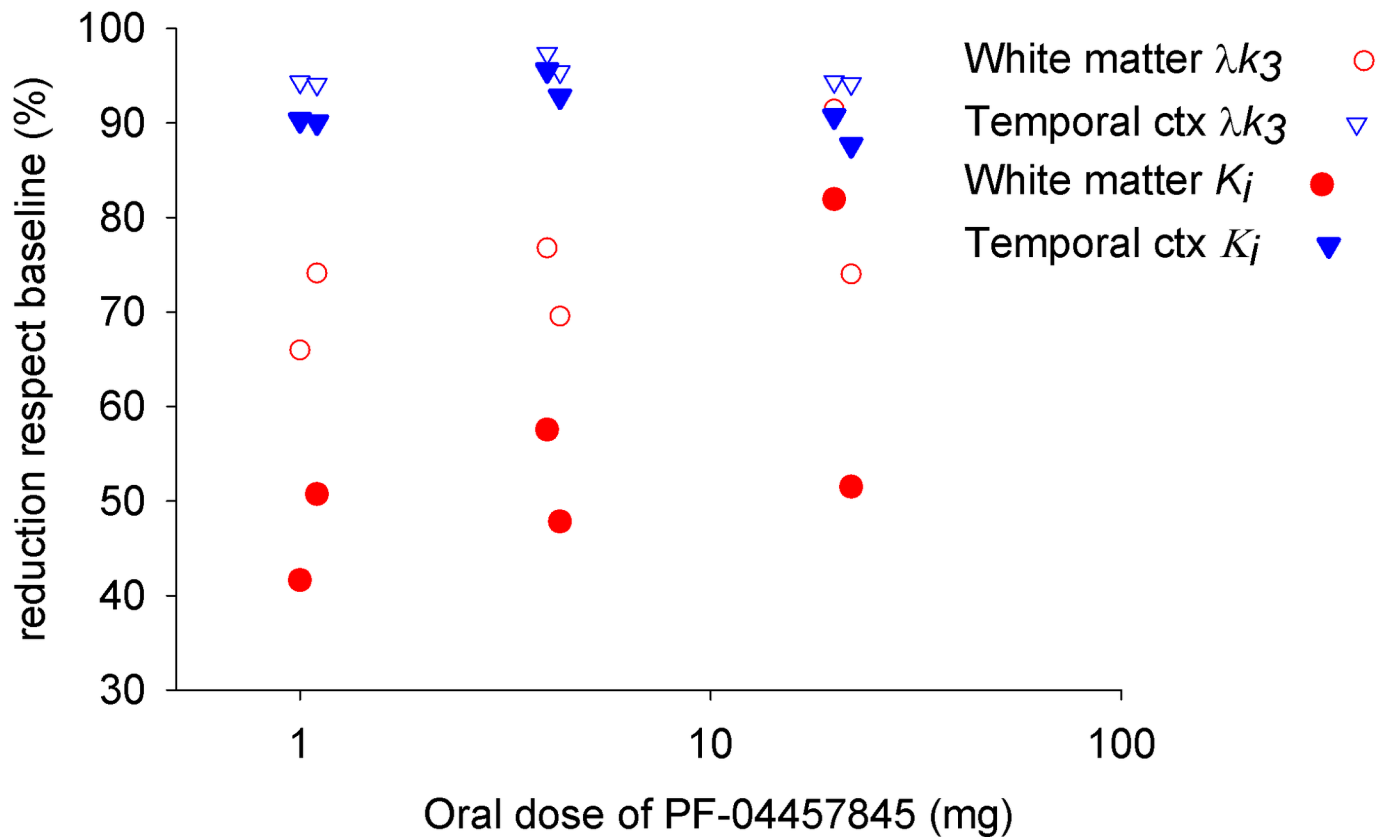
Fig 8. The change in FAAH activity, as measured with λk_3 (open symbols), following an oral dose of 1, 4 and 20 mg of PF-04457845 in the gray matter (temporal cortex) and white matter of 6 subjects. Solid symbols show the relative reduction of [^{11}C]CURB K_i in the same experiments. A small offset was applied for each oral dose in order to visualize overlapping symbols.

Discussion

The present work examined the bias induced by the noise when using BAFPIC to quantify voxel wise images of [^{11}C]CURB, a 2TCM irreversible radioligand. This work explicitly demonstrated the validation and limitations of the parametric maps of [^{11}C]CURB as a function of the range [$\theta_{min}, \theta_{max}$] when brain images are acquired with an HRRT and reconstructed using a FBP algorithm with Hann filter at Nyquist frequency.

The high level of noise in HRRT images does not allow for much flexibility in the selection of the member of the basis functions. The selection of [$\theta_{min}, \theta_{max}$] affects the shape of the distribution of probability of the parameters of interest (K_i and λk_3). Noise induces a systematic bias in the mean of the distribution of K_i and λk_3, which would underestimate differences in FAAH concentration. From a parametric mapping perspective, it is convenient to focus on K_i rather than λk_3. Variability of K_i is lower and the dependence of the bias with a change in B_{max} is lower. BAFPIC strongly reduces the variability of the standard method (Patlak plot).

For parametric maps, it is convenient to apply BAFPIC with V_B fixed rather than variable. At those high levels of noise, V_B does not present identifiability ($CoV\sim400\%$) its mean values are a function of the highest frequency in the basis (θ_{max}, c.f. section "high frequency components" in ref [13]) and the macroparameters derived when V_B is variable present higher variability. While a fixed V_B (e.g. to 5%) is incorrect in a voxel corresponding to a big artery (e.g. V_B = 100%), techniques of analysis of parametric images look for cluster of voxels rather than single voxels, thus

this error is nearly negligible. It should be noted that in the graphical methods for parametric mapping (i.e. Patlak or Logan plot), it is common practice to either ignore or subtract the vascular contribution with a fixed V_B value from the TAC prior to the application of the model.

An exaggerated selection for the slowest frequencies (e.g. θ_{min} = 0.01 min^{-1}) will produce non-normal distributions of K_i and λk_3 with a mean presenting significant underestimations. Our results are consistent with previous work that has shown: 1) that the spectral analysis method is known to be affected by the cutoff for slow frequencies[15] and 2) that using SRTM (BFM), the non-normal distribution of rate constants using BF can be observed for k'_2 [25].

Based on the simulations, we found that the parametric images of K_i can be generated with BAFPIC using constant V_B (= 5%) and a BF of $n \geq 50$ members with *frequencies* distributed logarithmically within [0.06, 3] min^{-1}. Consistently, our real images demonstrated that these settings were useful to look at 90% changes in the gray matter. Despite having a lower ability to quantify similar changes in the white matter, the potential of the parametric maps analysis was illustrated after the revelation of results in the white matter following FAAH inhibition with PF-04457845 that were not hypothesized in the ROI analysis. In clinical populations, in which changes in B_{max} are expected to be moderate (e.g. subjects with single nucleotide polymorphism (rs324420, C385A) show 23% lower [^{11}C]CURB binding (λk_3) in brain[26]), it is expected that those settings for BAFPIC will work well for both gray and white matter ROIs. However, the results presented in this work will eventually allow to customize the BAFPIC parameters for different scenarios (macroparameters, expected values of rate constants based on rCBF, V_{ND} and B_{max}), while understanding the limitations.

The mathematical expression in the 2TCMi of λk_3 has advantages over K_i a) it is proportional to k_3 (B_{max}), and b) it does not depend explicitly on rCBF. Despite the fact that all the irreversible radiotracers can suffer from delivery limitation effects, the proportion between rate constant ($k_3 \sim k_2/2$) for healthy controls is such that in the gray matter, [^{11}C]CURB binding is not sensitive to rCBF. The white matter ($k_3 \sim k_2$) might be more compromised; however, the TACs still present a peak followed by a plateau that allows to differentiate the contribution of the delivery and specific binding. In contrast, K_i is, by definition, affected by rCBF. In [^{11}C]CURB, its effect is not strong: a significant change of rCBF from 90 mL·100 mL^{-1}·min^{-1} (K_1 = 0.28 mL·cm^{-3}·min^{-1}) to 40 mL·100 mL^{-1}·min^{-1} (K_1 = 0.22 mL·cm^{-3}·min^{-1})[1] would reduce K_i by 10% (using a high V_{ND} = 4 ml·cm^{-3} and k_3^p). When expected changes in rCBF may affect the interpretation of the results of a study, parametric maps of λk_3 are still feasible but the optimal range for the BF is [0.06, 0.5] min^{-1}. However, the statistical power will decrease as a consequence of the increase in variability and bias correlated with k_3 values.

There is a discrepancy between the simulation and the real data regarding V_{ND}. Fig 5 seems to indicate that the real data in the baseline condition ($V_{ND} \sim 3$ mL·cm^{-3}) corresponds to the simulated data with V_{ND} = 4.5 mL·cm^{-3}. We have also observed in the ROI analysis that 1) V_{ND} in the blocked condition is slightly higher[2], 2) with >90% specific binding blocked 2TCMi still fits the TACs better than 1TCM, 3) 1TCM model of the blocked TAC gives a slightly higher V_{ND}. Therefore, the simulated TACs with 2TCMi (1 reversible compartment for non displaceable binding and other irreversible for specific binding) could be an oversimplification. On the other hand, a straightforward comparison may be affected by a number of factors: 1) simulated changes in V_{ND} kept k_3 fixed and simulated changes in B_{max} kept k_2 fixed, but in our experiments we noted that k_2 correlated with k_3 in healthy controls, 2) while data points in the simulation were weighted based on Eq 5, in the real data true concentration C_i is unknown, thus the weight is based on trues in the field of view, 3) simulated noise level could overestimate/underestimate the noise level of the HRRT, 4) tissue heterogeneity in the ROI could affect the comparison between parametric maps and ROI results.

The results presented here for TACs with intermediate noise level can be applied to [^{11}C] CURB images acquired with different scanners or algorithms for reconstruction. However, it should be noted that the simulations presented here assumed Gaussian noise, which eventually may not be the case for images coming from other algorithms of reconstruction (e.g. non-negative constrained iterative algorithm when the number of counts in detectors is low).

The present results can provide a guideline for application to other radioligands; however, every radioligand will require an independent validation. For example, for a radioligand with a slower delivery to tissue, the vascular component may be more visible in the TAC and V_B can be fitted.

Conclusion

BAFPIC with constant V_B can be used to generate K_i parametric maps of [^{11}C]CURB images acquired with the HRRT provided that the range of the BF is carefully adjusted. The noise induces an underestimation proportional to the FAAH concentration, which will reduce the potential differences between groups. Thus, BAFPIC reduces more than 60% the variability relative to the Patlak plot. While λk_3 parametric maps are feasible, they present higher bias and variability. In images with lower noise (e.g. different scanner or reconstruction algorithm) these effects will decrease.

Supporting information

S1 Fig. Noise induced variability expressed as CoV = 100%*Stdev/mean for K_i and λk_3 as a function of k_3/k_3^P for BAFPIC with different ranges of the exponent θ of the basis function compared to Patlak plot. The simulated noise in the TACs is similar to the noise regularly observed at the HRRT voxel level ($sf = 120$).
(TIF)

S2 Fig. Noise induced variability expressed as Stdev for K_i and λk_3 as function of k_3/k_3^P for BAFPIC with different ranges of the exponent θ of the basis function compared to Patlak plot. The simulated noise in the TACs is similar to the noise regularly observed at the HRRT voxel level ($sf = 120$).
(TIF)

S3 Fig. Noise induced bias for K_i and λk_3 as function of k_3/k_3^P for BAFPIC with different ranges of the exponent θ of the basis function compared to Patlak plot. The simulated noise in the TACs is similar to the noise regularly observed at the HRRT voxel level ($sf = 120$). Bias is computed as (measured-simulated). c.f. Fig 3 in manuscript. Note that yellow line in this figure corresponds with yellow line in Fig 4 in manuscript.
(TIF)

S4 Fig. Histograms of K_i values in the cerebellar cortex of a single subject parametric map. Comparison of the distribution produced by BAFPIC ($V_B = 5\%$) $\theta = [0.06, 3]$ min^{-1}, BAFPIC ($V_B = 5\%$) $\theta = [0.01, 3]$ min^{-1}, and Patlak plot. The mean values are indicated with triangles together with the K_i estimation from 2TCMi for the ROI analysis. While the Patlak distribution presents no bias, it shows a higher variability. The skewed distribution for BAFPIC ($V_B = 5\%$), $\theta = [0.01, 3]$ min^{-1} produce a large bias in the mean values of the distribution. BAFPIC ($V_B = 5\%$), $\theta = [0.06, 3]$ min^{-1} gives a tradeoff between bias and variability.
(TIF)

S1 File. Monte Carlo simulations. This MS-Excel file contains all the simulations performed.
(XLSX)

Acknowledgments

Author Contributions

Conceptualization: Pablo M. Rusjan.

Data curation: Pablo M. Rusjan, Dunja Knezevic.

Formal analysis: Pablo M. Rusjan.

Funding acquisition: Isabelle Boileau, Junchao Tong, Sylvain Houle.

Investigation: Pablo M. Rusjan, Isabelle Boileau, Junchao Tong.

Methodology: Pablo M. Rusjan.

Project administration: Pablo M. Rusjan.

Resources: Isabelle Boileau, Junchao Tong, Sylvain Houle.

Software: Pablo M. Rusjan.

Supervision: Pablo M. Rusjan, Isabelle Boileau, Junchao Tong, Romina Mizrahi, Alan A. Wilson, Sylvain Houle.

Validation: Pablo M. Rusjan.

Visualization: Pablo M. Rusjan.

Writing – original draft: Pablo M. Rusjan, Dunja Knezevic, Isabelle Boileau, Junchao Tong, Romina Mizrahi, Alan A. Wilson, Sylvain Houle.

Writing – review & editing: Pablo M. Rusjan, Dunja Knezevic, Isabelle Boileau, Junchao Tong, Romina Mizrahi, Alan A. Wilson, Sylvain Houle.

References

1. Rusjan PM, Wilson AA, Mizrahi R, Boileau I, Chavez SE, Lobaugh NJ, et al. Mapping human brain fatty acid amide hydrolase activity with PET. J Cereb Blood Flow Metab. 2013; 33(3):407–14. https://doi.org/10.1038/jcbfm.2012.180 PMID: 23211960; PubMed Central PMCID: PMCPMC3587811.

2. Boileau I, Rusjan PM, Williams B, Mansouri E, Mizrahi R, De Luca V, et al. Blocking of fatty acid amide hydrolase activity with PF-04457845 in human brain: a positron emission tomography study with the novel radioligand [C]CURB. J Cereb Blood Flow Metab. 2015. https://doi.org/10.1038/jcbfm.2015.133 PMID: 26082009.

3. Koeppe RA, Frey KA, Snyder SE, Meyer P, Kilbourn MR, Kuhl DE. Kinetic modeling of N-[11C]methylpiperidin-4-yl propionate: alternatives for analysis of an irreversible positron emission tomography trace for measurement of acetylcholinesterase activity in human brain. J Cereb Blood Flow Metab. 1999; 19 (10):1150–63. https://doi.org/10.1097/00004647-199910000-00012 PMID: 10532640.

4. Johnson DS, Stiff C, Lazerwith SE, Kesten SR, Fay LK, Morris M, et al. Discovery of PF-04457845: A Highly Potent, Orally Bioavailable, and Selective Urea FAAH Inhibitor. ACS medicinal chemistry letters. 2011; 2(2):91–6. https://doi.org/10.1021/ml100190t PMID: 21666860; PubMed Central PMCID: PMC3109749.

5. Ahn K, Smith SE, Liimatta MB, Beidler D, Sadagopan N, Dudley DT, et al. Mechanistic and pharmacological characterization of PF-04457845: a highly potent and selective fatty acid amide hydrolase inhibitor that reduces inflammatory and noninflammatory pain. The Journal of pharmacology and experimental therapeutics. 2011; 338(1):114–24. https://doi.org/10.1124/jpet.111.180257 PMID: 21505060; PubMed Central PMCID: PMC3126636.

6. Rizzo G, Turkheimer FE, Keihaninejad S, Bose SK, Hammers A, Bertoldo A. Multi-Scale hierarchical generation of PET parametric maps: application and testing on a [11C]DPN study. Neuroimage. 2012; 59(3):2485–93. https://doi.org/10.1016/j.neuroimage.2011.08.101 PMID: 21924366.

7. Patlak CS, Blasberg RG, Fenstermacher JD. Graphical evaluation of blood-to-brain transfer constants from multiple-time uptake data. J Cereb Blood Flow Metab. 1983; 3(1):1–7. https://doi.org/10.1038/jcbfm.1983.1 PMID: 6822610.

8. Yu DC, Huang SC, Barrio JR, Phelps ME. The assessment of the non-equilibrium effect in the 'Patlak analysis' of Fdopa PET studies. Phys Med Biol. 1995; 40(7):1243–54. PMID: 7568380.

9. Alpert NM, Eriksson L, Chang JY, Bergstrom M, Litton JE, Correia JA, et al. Strategy for the measurement of regional cerebral blood flow using short-lived tracers and emission tomography. J Cereb Blood Flow Metab. 1984; 4(1):28–34. https://doi.org/10.1038/jcbfm.1984.4 PMID: 6607259.

10. Koeppe RA, Holden JE, Ip WR. Performance comparison of parameter estimation techniques for the quantitation of local cerebral blood flow by dynamic positron computed tomography. J Cereb Blood Flow Metab. 1985; 5(2):224–34. https://doi.org/10.1038/jcbfm.1985.29 PMID: 3872874.

11. Gunn RN, Lammertsma AA, Hume SP, Cunningham VJ. Parametric imaging of ligand-receptor binding in PET using a simplified reference region model. Neuroimage. 1997; 6(4):279–87. https://doi.org/10.1006/nimg.1997.0303 PMID: 9417971.

12. Hong YT, Beech JS, Smith R, Baron JC, Fryer TD. Parametric mapping of [18F]fluoromisonidazole positron emission tomography using basis functions. J Cereb Blood Flow Metab. 2011; 31(2):648–57. https://doi.org/10.1038/jcbfm.2010.141 PMID: 20736963; PubMed Central PMCID: PMCPMC3049519.

13. Cunningham VJ, Jones T. Spectral analysis of dynamic PET studies. J Cereb Blood Flow Metab. 1993; 13(1):15–23. https://doi.org/10.1038/jcbfm.1993.5 PMID: 8417003.

14. Gunn RN, Gunn SR, Turkheimer FE, Aston JA, Cunningham VJ. Positron emission tomography compartmental models: a basis pursuit strategy for kinetic modeling. J Cereb Blood Flow Metab. 2002; 22(12):1425–39. https://doi.org/10.1097/01.wcb.0000045042.03034.42 PMID: 12468888.

15. Hammers A, Asselin MC, Turkheimer FE, Hinz R, Osman S, Hotton G, et al. Balancing bias, reliability, noise properties and the need for parametric maps in quantitative ligand PET: [(11)C]diprenorphine test-retest data. Neuroimage. 2007; 38(1):82–94. https://doi.org/10.1016/j.neuroimage.2007.06.035 PMID: 17764977.

16. Innis RB, Carson R. Consensus nomenclature: its time has come. Eur J Nucl Med Mol Imaging. 2007; 34(8):1239. Epub 2007/05/18. https://doi.org/10.1007/s00259-007-0481-7 PMID: 17508212.

17. Gunn RN, Gunn SR, Cunningham VJ. Positron emission tomography compartmental models. J Cereb Blood Flow Metab. 2001; 21(6):635–52. https://doi.org/10.1097/00004647-200106000-00002 PMID: 11488533.

18. Hong YT, Fryer TD. Kinetic modelling using basis functions derived from two-tissue compartmental models with a plasma input function: general principle and application to [18F]fluorodeoxyglucose positron emission tomography. NeuroImage. 51(1):164–72. Epub 2010/02/17. doi: S1053-8119(10)00181-3 [pii] https://doi.org/10.1016/j.neuroimage.2010.02.013 PMID: 20156574.

19. Logan J, Fowler JS, Volkow ND, Ding YS, Wang GJ, Alexoff DL. A strategy for removing the bias in the graphical analysis method. J Cereb Blood Flow Metab. 2001; 21(3):307–20. Epub 2001/04/11. https://doi.org/10.1097/00004647-200103000-00014 PMID: 11295885.

20. Ichise M, Toyama H, Innis RB, Carson RE. Strategies to improve neuroreceptor parameter estimation by linear regression analysis. J Cereb Blood Flow Metab. 2002; 22(10):1271–81. https://doi.org/10.1097/01.WCB.0000038000.34930.4E PMID: 12368666.

21. Bencherif B, Stumpf MJ, Links JM, Frost JJ. Application of MRI-based partial-volume correction to the analysis of PET images of mu-opioid receptors using statistical parametric mapping. J Nucl Med. 2004; 45(3):402–8. Epub 2004/03/06. PMID: 15001679.

22. Rusjan PM, Wilson AA, Miler L, Fan I, Mizrahi R, Houle S, et al. Kinetic modeling of the monoamine oxidase B radioligand [(1)(1)C]SL25.1188 in human brain with high-resolution positron emission tomography. J Cereb Blood Flow Metab. 34(5):883–9. Epub 2014/02/13. doi: jcbfm201434 [pii] https://doi.org/10.1038/jcbfm.2014.34 PMID: 24517979; PubMed Central PMCID: PMC4013770.

23. Ito H, Kanno I, Kato C, Sasaki T, Ishii K, Ouchi Y, et al. Database of normal human cerebral blood flow, cerebral blood volume, cerebral oxygen extraction fraction and cerebral metabolic rate of oxygen measured by positron emission tomography with ^{15}O-labelled carbon dioxide or water, carbon monoxide and oxygen: a multicentre study in Japan. Eur J Nucl Med Mol Imaging. 2004; 31(5):635–43. https://doi.org/10.1007/s00259-003-1430-8 PMID: 14730405

24. Lammertsma AA. Compartmental Modeling in Emission Tomography. Handbook of Particle Detection and Imaging: Springer Berlin Heidelberg; 2012. p. 1065–81.

25. Wu Y, Carson RE. Noise reduction in the simplified reference tissue model for neuroreceptor functional imaging. J Cereb Blood Flow Metab. 2002; 22(12):1440–52. https://doi.org/10.1097/01.WCB.0000033967.83623.34 PMID: 12468889.

26. Boileau I, Tyndale RF, Williams B, Mansouri E, Westwood DJ, Le Foll B, et al. The fatty acid amide hydrolase C385A variant affects brain binding of the positron emission tomography tracer [11C]CURB. J Cereb Blood Flow Metab. 2015; 35(8):1237–40. https://doi.org/10.1038/jcbfm.2015.119 PMID: 26036940; PubMed Central PMCID: PMC4527995.